BNL-225955-2024-JAAM

Synthesis of 2H/fcc-Heterophase AuCu Nanostructures with high-index facets for Highly Efficient Electrochemical CO2 Reduction at Industrial Current Densities

X. Zhou, L. Ma

To be published in "Advanced Materials"

August 2023

Photon Sciences

Brookhaven National Laboratory

U.S. Department of Energy

USDOE Office of Science (SC), Basic Energy Sciences (BES)

DISCLAIMER

Synthesis of hierarchical 2H/*fcc*-heterophase AuCu nanostructures with high-index facets for highly efficient electrochemical CO_2 reduction at industrial current densities

Xichen Zhou[1‡], An Zhang[1‡], Bo Chen[1‡], Shangqian Zhu[4], Yu Cui[5], Licheng Bai[1,6], Jinli Yu[1], Qinbai Yun[1], Yiyao Ge[1], Lingwen Liao[1,7], Lujiang Li[1], Biao Huang[1,2], Qingbo Wa[1], Gang Wang[8], Long Zheng[8], Guangyao Liu[1], Jiawei Liu[9], Ye Chen[8], Jinlan Wang[5], Zhanxi Fan[1,2,3], Chongyi Ling[5], Yonghua Du[10], Minhua Shao[4,11], Hua Zhang[1,2,3*]

[1]Department of Chemistry, City University of Hong Kong, Hong Kong, China.

[2]Hong Kong Branch of National Precious Metals Material Engineering Research Center (NPMM), City University of Hong Kong, Hong Kong, China.

[3]Shenzhen Research Institute, City University of Hong Kong, Shenzhen, 518057, China.

[4]Department of Chemical and Biomolecular Engineering, The Hong Kong University of Science and Technology, Hong Kong, China.

[5]School of Physics, Southeast University, Nanjing, 211189, China.

[6]Materials Interfaces Center, Shenzhen Institute of Advanced Technology, Chinese Academy of Sciences, Shenzhen, 518057, China.

[7]Key Laboratory of Materials Physics, Anhui Key Laboratory of Nanomaterials and Nanotechnology, Institute of Solid State Physics, Chinese Academy of Sciences, Hefei, 230031, China.

[8]Department of Chemistry, The Chinese University of Hong Kong, Hong Kong, China.

[9]Center for Programmable Materials, School of Materials Science and Engineering, Nanyang Technological University, Singapore 639798, Singapore.

[10] National Synchrotron Light Source II, Brookhaven National Laboratory, Upton, NY 11973, USA.

[11]Energy Institute, Hong Kong Branch of the Southern Marine Science and Engineering Guangdong Laboratory, and Chinese National Engineering Research Center for Control & Treatment of Heavy Metal Pollution, The Hong Kong University of Science and Technology, Hong Kong, China.

‡X. Z., A. Z., and B. C. contributed equally to this work.

*Corresponding author.

Email address:

hua.zhang@cityu.edu.hk

Abstract

Structural engineering of nanomaterials offers a promising way for developing high-performance catalysts towards sustainable catalysis. However, the delicate modulation of thermodynamically unfavorable nanostructures with unconventional phases still remains a challenge. Here, we report the synthesis of hierarchical AuCu nanostructures with hexagonal close-packed (2H-type)/face-centered cubic (*fcc*) heterophase, high-index facets, planar defects (*e.g.*, stacking faults, twin boundaries, and grain boundaries), and tunable Cu content. The obtained 2H/*fcc* $Au_{99}Cu_1$ exhibits excellent performance for the electrocatalytic CO_2 reduction to produce CO, outperforming the 2H/*fcc* $Au_{91}Cu_9$ and *fcc* $Au_{99}Cu_1$. Our experimental results, especially that obtained by *in situ* attenuated total reflection Fourier-transform infrared spectroscopy, suggest that the enhanced catalytic performance of 2H/*fcc* $Au_{99}Cu_1$ arises from the unconventional 2H/*fcc* heterophase, high-index facets, planar defects, and appropriate alloying of Cu. Impressively, the 2H/*fcc* $Au_{99}Cu_1$ shows CO Faradaic efficiencies of 96.6% and 92.6% at industrial current densities of 300 mA cm^{-2} and 500 mA cm^{-2}, respectively, placing it among the best CO_2 reduction electrocatalysts for CO production. Our atomically structural regulation based on phase engineering of nanomaterials (PEN) provides an avenue for the rational design and preparation of high-performance electrocatalysts for various sustainable catalytic applications.

Introduction

Delicately structural modulation of metal nanostructures has been demonstrated as a feasible and effective way to regulate their physicochemical properties and promote their performance in various applications, especially in catalysis[1-4]. Over the past decades, it has been found that diverse structural features, including composition[3-6], defect[7], morphology[1,8-10], and arrangement of surface atoms[11-14], play roles in determining the catalytic properties of metal nanomaterials. In particular, the hierarchical morphologies can endow metal nanostructures with more exposed active sites and make the nanostructures more accessible to the reactants, which are of great importance for gas-related heterogeneous catalytic reactions, such as electrochemical CO_2 reduction reaction (CO_2RR)[15]. In addition, high-index facets with highly unsaturated coordination environments can modulate the surface electronic structure of metal nanomaterials and thus optimize the adsorption/desorption behaviors of intermediate species, resulting in excellent catalytic activities[11,12]. For example, the high-index (211) facet of Au exhibited superior current density towards the electrochemical CO_2RR to CO, which is about 20-fold higher than that measured on the low-index (100) facet of Au[13]. However, until now, the structural engineering of metal nanomaterials has mainly focused on those with thermodynamically stable phases. Phase engineering of nanomaterials (PEN) has been considered as one of the emerging strategies to design and prepare novel nanostructures with intriguing physicochemical properties and compelling performances for diverse applications[16-18]. Briefly, PEN focuses on the delicate regulation of atomic arrangement in materials, which could

result in the formation of novel nanomaterials with unconventional crystal phases[19-21], amorphous phase[22,23], and heterophases[24-27]. Among them, heterophase-metal nanomaterials constructed by two or more phases have attracted increasing attention owing to the synergistic effect between different phases and the unique phase boundaries[24-28]. To date, heterophase-metal nanomaterials have demonstrated promising catalytic applications in hydrogenation reaction[27], hydrogen evolution reaction[28,29], oxygen evolution reaction[30], ethanol oxidation reaction[24,31], *etc.* Notably, the heterophase-Au nanorods have been used as effective catalysts for the electrochemical CO_2RR[25,32]. However, due to the thermodynamically unfavored nature, it still remains challenging to delicately modulate the composition, architecture, defect, and exposed facets of heterophase Au-based nanomaterials for further enhancing their electrocatalytic performance towards CO_2RR at industrial current densities.

In this work, we report a facile wet-chemical method for the synthesis of hexagonal close-packed (2H-type)/face-centered cubic (*fcc*)-heterophase AuCu nanostructures with a hierarchical architecture. The obtained hierarchical 2H/*fcc* AuCu nanostructures can be used as excellent electrocatalysts for highly efficient electrochemical CO_2RR towards CO production. In particular, the 2H/*fcc* $Au_{99}Cu_1$ shows superior CO_2RR performance compared to the 2H/*fcc* $Au_{91}Cu_9$ and *fcc* $Au_{99}Cu_1$. Impressively, by using a flow cell electrolyzer, the 2H/*fcc* $Au_{99}Cu_1$ exhibits CO Faradaic efficiencies (FEs) of 96.6% and 92.6% at industrial current densities of 300 mA cm^{-2} and 500 mA cm^{-2}, respectively, placing it among the best reported CO_2RR catalysts for CO production. Furthermore, our experimental results, including that obtained by *in situ* attenuated total

reflection Fourier-transform infrared (ATR-FTIR) spectroscopy, reveal that the remarkable CO_2RR performance stems from the unique structure of 2H/*fcc* $Au_{99}Cu_1$, including the unconventional 2H/*fcc* heterophase, high-index facets, planar defects (*e.g.,* stacking faults, twin boundaries, and grain boundaries), and appropriate alloying of Cu.

Synthesis and characterization

Two 2H/*fcc*-heterophase AuCu nanostructures, *i.e.*, $Au_{99}Cu_1$ and $Au_{91}Cu_9$, were synthesized *via* a facile one-pot wet-chemical approach at different reaction time. Briefly, the $Au_{99}Cu_1$ was prepared by reducing Au(III) chloride trihydrate in an oleylamine solution containing amantadine hydrochloride and Cu(II) chloride dihydrate at 80 ℃ for 8 h (see Supporting Information for details). The obtained $Au_{99}Cu_1$ contains a small amount of Cu with an atomic ratio of 99/1 for Au/Cu, which is revealed by inductively coupled plasma optical emission spectrometry (ICP-OES). The energy dispersion X-ray spectroscopy (EDS) mapping (Fig. S1) shows that Cu uniformly distributes in the $Au_{99}Cu_1$. Transmission electron microscopy (TEM, Fig. 1a and Figs. S2 and S3) and dark-field scanning TEM (STEM, Fig. S4) images exhibit that the $Au_{99}Cu_1$ possesses a unique hierarchical architecture composed of ultrathin nanosheets with protruding edges, as schematically illustrated in Fig. 1b. The as-synthesized $Au_{99}Cu_1$ possesses a lateral size of up to hundreds of nanometers (Figs. S2-S4), and the thickness of the nanosheets in $Au_{99}Cu_1$ is estimated to be 2.2±0.4 nm by measuring the nanosheets standing vertically on the TEM grid (Figs. S5 and S6).

Fig. 1c shows the spherical aberration-corrected high-angle annular dark-field STEM (HAADF-STEM) image of a protrusion at the edge of $Au_{99}Cu_1$, in which two distinct

types of atomic arrangements along the close-packed directions of 2H and *fcc* phases, *i.e.*, $[001]_h$ and $[11\bar{1}]_f$, respectively, can be clearly observed. Selected-area fast Fourier transform (FFT) patterns taken from the protrusion match well with the diffraction patterns of the 2H phase along the $[110]_h$-zone axis (Fig. 1d, f) and *fcc* phase along the $[101]_f$-zone axis (Fig. 1e), respectively. A characteristic atomic stacking sequence of "AB" is displayed in the 2H part (Fig. 1g), and an atomic stacking sequence of "ABC" is observed in the *fcc* part (Fig. 1h). In addition, the $(002)_h$ planes in 2H domain exhibit an average interplanar spacing of 2.35 Å, while the $(11\bar{1})_f$ planes in *fcc* domain show a slightly smaller average interplanar spacing of 2.32 Å (Fig. S7). The distinct phase arrangements in the $Au_{99}Cu_1$ verify the formation of an unconventional 2H/*fcc* heterophase, which is further corroborated by the XRD pattern (Fig. S8).

Due to the protruding edges of the ultrathin 2H/*fcc* nanosheets, the 2H/*fcc* $Au_{99}Cu_1$ possesses abundant stepped surface. The atomic-resolution HAADF-STEM images viewed along the $[110]_h$/$[101]_f$-zone axis in Fig. 1i,j and Figs. S9-S11 show the atomic arrangement on the edge surfaces of the 2H and *fcc* domains. Different from the low-index *fcc* $(11\bar{1})$ facet with smooth surface (Fig. 1k and Fig. S11g), there are stepped surfaces on the protruding edges (Fig. 1i,j and Figs. S9-S11). In particular, high-index facets in the unconventional 2H domain, including $(3\bar{3}4)_h$ (Fig. 1l), $(2\bar{2}3)_h$, $(1\bar{1}3)_h$, and $(1\bar{1}2)_h$ (Figs. 1i,j, S9b, and S10c), and the *fcc* phase, such as $(35\bar{3})_f$, $(31\bar{3})_f$, $(\bar{2}\bar{1}2)_f$, $(13\bar{1})_f$, and $(12\bar{1})_f$ (Fig. S11h-j), can be observed on the stepped surfaces. Apart from the stepped edge surface, abundant planar defects, including stacking faults, twin boundaries, and grain boundaries, can be observed in 2H/*fcc* $Au_{99}Cu_1$ (Fig. 1c and Figs.

S9-S12). Note that the stacking faults and twin boundaries are perpendicular to the close-packed $[001]_h/[11\bar{1}]_f$ direction.

In addition, the $Au_{91}Cu_9$ nanostructure with an atomic ratio of 91/9 for Au/Cu, measured by ICP-OES, has also been prepared by prolonging the reaction time from 8 h used for the preparation of $Au_{99}Cu_1$ to 48 h (see Supporting Information for details). The obtained $Au_{91}Cu_9$ presents a three-dimensional network architecture composed of one-dimensional worm-like nanostructures (Fig. 2a,b). As shown in the spherical aberration-corrected HAADF-STEM image (Fig. 2c) and corresponding FFT patterns (Fig. 2d-f) collected from the selected areas, the $Au_{91}Cu_9$ also displays a unique 2H/*fcc* heterophase with atomically sharp phase boundaries, showing the alternating arrangements of 2H and *fcc* phases along the close-packed $[001]_h/[11\bar{1}]_f$ direction. The 2H/*fcc* heterophase of $Au_{91}Cu_9$ can be further confirmed by the XRD characterization (Fig. S13). Moreover, 2H/*fcc* $Au_{91}Cu_9$ exhibits various planar defects in the 2H and *fcc* domains, *e.g.*, stacking faults, twin boundaries, and grain boundaries. Note that the stacking faults and twin boundaries in 2H/*fcc* $Au_{91}Cu_9$ are perpendicular to the close-packed $[001]_h/[11\bar{1}]_f$ direction (Fig. 2c). Moreover, as shown in the spherical aberration-corrected HAADF-STEM images viewed along the $[110]_h/[101]_f$-zone axis, the edges of 2H/*fcc* $Au_{91}Cu_9$ possess various high-index facets, such as $(3\bar{3}4)_h$, $(3\bar{3}2)_h$, $(\bar{2}23)_h$, $(2\bar{2}1)_h$, $(\bar{1}14)_h$, $(\bar{1}13)_h$, and $(\bar{1}12)_h$, in the 2H parts (Fig. 2g,h). In addition, the EDS mapping results (Fig. 2i-l) suggest that the Au and Cu are uniformly distributed in the 2H/*fcc* $Au_{91}Cu_9$. On the basis of the aforementioned characterizations, the model of the as-synthesized 2H/*fcc* $Au_{91}Cu_9$ can be schematically illustrated in Fig. 2m.

To unravel the chemical states of Cu and Au elements in the synthesized 2H/*fcc* AuCu nanostructures, X-ray photoelectron spectroscopy (XPS) characterizations were conducted. The Cu 2p peaks in Fig. 3a indicate that Cu is mainly in the metallic state (Cu^0) or Cu^{1+} state in the 2H/*fcc* $Au_{99}Cu_1$ and $Au_{91}Cu_9$, which is consistent with a previously reported result[33]. The slight shift (~0.7 eV) of Cu 2p peaks towards higher binding energies with the increase of Cu content (Fig. 3a) is also consistent with previous reports on the AuCu alloy[6,34]. To further distinguish the Cu^0 and Cu^{1+} states in the 2H/*fcc* $Au_{99}Cu_1$ and $Au_{91}Cu_9$, the Cu Auger electron spectroscopy (AES) measurement was carried out. As shown in the Cu LMM AES spectra (Fig. 3b), the Cu in 2H/*fcc* $Au_{99}Cu_1$ mainly possesses metallic state, while the 2H/*fcc* $Au_{91}Cu_9$ has both Cu^0 and Cu^{1+} species[35]. The Au 4f spectra in Fig. 3c demonstrate that Au in both 2H/*fcc* $Au_{99}Cu_1$ and $Au_{91}Cu_9$ is in metallic state[36]. Due to the electron interaction between Au and Cu species, the Au 4f peaks of 2H/*fcc* AuCu slightly shift (~0.5 eV) to higher binding energies as the atomic ratio of Cu/Au increases[34,37]. Furthermore, X-ray absorption spectroscopy (XAS) was employed to reveal the electronic structures of the 2H/*fcc*-heterophase AuCu. In the Au L_3-edge X-ray absorption near-edge structure (XANES) spectra (Fig. 3d), both 2H/*fcc* $Au_{99}Cu_1$ and 2H/*fcc* $Au_{91}Cu_9$ exhibit similar white line intensity and XANES energy as compared to the Au foil used as reference. The Fourier-transformed extended X-ray absorption fine structure (FT-EXAFS) spectra of the 2H/*fcc* $Au_{99}Cu_1$ and 2H/*fcc* $Au_{91}Cu_9$ show similar peak positions with the Au foil (Fig. 3e), indicating their similar Au-Au bond lengths. These results demonstrate that the Au element in the as-prepared 2H/*fcc* $Au_{99}Cu_1$ and 2H/*fcc* $Au_{91}Cu_9$ is predominantly

in the metallic state, consistent with the XPS result (Fig. 3c). Moreover, in the FT-EXAFS spectra of Au L3-edge (Fig. 3e), the peak intensities of the 2H/*fcc* $Au_{99}Cu_1$ and 2H/*fcc* $Au_{91}Cu_9$ are lower than that of Au foil, indicating the lower coordination environment of Au in our synthesized 2H/*fcc* AuCu nanostructures[38].

Electrochemical CO_2 reduction

As a proof-of-concept application, our synthesized 2H/*fcc* AuCu nanostructures were used as novel catalysts for electrochemical CO_2RR. To gain insight into the structure-dependent CO_2RR performance, *fcc* $Au_{99}Cu_1$ nanostructure (Figs. S14-S16) was prepared and used for comparison. First, we evaluated the CO_2RR performance of the 2H/*fcc* $Au_{99}Cu_1$, 2H/*fcc* $Au_{91}Cu_9$, and *fcc* $Au_{99}Cu_1$ catalysts in the CO_2-saturated 0.5 M $KHCO_3$ aqueous solution under ambient condition by using a H-type cell. As displayed in Fig. 4a, the 2H/*fcc* $Au_{99}Cu_1$ exhibits high FEs of over 95% towards CO production in a wide potential window from -0.5 to -0.8 V (*vs.* reversible hydrogen electrode, RHE). Remarkably, the 2H/*fcc* $Au_{99}Cu_1$ can reach the highest CO FE of 99.7% at a low potential of -0.5 V (*vs.* RHE), indicating a near-complete suppression of the competing hydrogen evolution reaction (Fig. S17). In comparison, the 2H/*fcc* $Au_{91}Cu_9$ shows the highest CO FE of 82.7% at -0.7 V (*vs.* RHE) (Fig. 4a). It is worth mentioning that the presence of 9.0% of Cu, including Cu^0 and Cu^{1+} species, in 2H/*fcc* $Au_{91}Cu_9$ can generate C_2H_4 during CO_2RR, showing a FE of 16.8% at -1.0 V (*vs.* RHE) (Fig. S18). These results suggest that tuning the Cu content of the synthesized 2H/*fcc* AuCu nanostructures can significantly change the selectivity of their CO_2RR. Moreover, the *fcc* $Au_{99}Cu_1$ possesses a maximum CO FE of 90.2% at -0.8 V (*vs.* RHE) and a low CO

FE of only 68.3% at -0.5 V (*vs.* RHE), which are much lower compared to those of the 2H/*fcc* $Au_{99}Cu_1$, indicating that the unique 2H/*fcc* heterophase plays a key role in achieving the high CO selectivity of CO_2RR. Moreover, the linear sweep voltammetry (LSV) measurements show that the 2H/*fcc* $Au_{99}Cu_1$ and 2H/*fcc* $Au_{91}Cu_9$ deliver larger current densities compared to the *fcc* $Au_{99}Cu_1$ (Fig. S19). Remarkably, the 2H/*fcc* $Au_{99}Cu_1$ possesses the highest geometric CO partial current density (J_{CO}) in the entire potential window from -0.4 to -1.0 V (*vs.* RHE) (Fig. 4b). The superior performance of the 2H/*fcc* $Au_{99}Cu_1$ toward the CO production places it among the best reported Au-based electrocatalysts for CO_2RR to produce CO in the H-type cell (Table S1).

The reaction kinetics of the catalysts was investigated by the Tafel analysis. The Tafel slopes were obtained by plotting the overpotential against the logarithm of J_{CO}. As illustrated in Fig. 4c, the Tafel slope of 2H/*fcc* $Au_{99}Cu_1$ is 81.4 mV dec^{-1}, which is smaller than those of 2H/*fcc* $Au_{91}Cu_9$ (88.5 mV dec^{-1}) and *fcc* $Au_{99}Cu_1$ (92.9 mV dec^{-1}). It suggests that all the catalysts share the same CO_2RR pathway, *i.e.*, a fast one-electron transfer process takes place to generate adsorbed $CO_2^{\bullet-}$ which then combines with a proton to form adsorbed COOH as the rate-determining step[39,40]. The smaller Tafel slope of 2H/*fcc* $Au_{99}Cu_1$ reveals a faster reaction kinetics compared to the other two catalysts.

In situ electrochemical ATR-FTIR spectroscopy was further conducted to monitor the CO_2RR process over the 2H/*fcc* $Au_{99}Cu_1$ and 2H/*fcc* $Au_{91}Cu_9$. The ATR-FTIR spectra were collected with the potential stepping from -0.25 to -0.90 V (*vs.* RHE) in a CO_2-saturated 0.5 M $KHCO_3$ aqueous solution. As presented in Fig. 4d,e, the downward

absorption bands centered at 2342 cm^{-1} and the strong upward absorption bands located at 1400 cm^{-1} of both catalysts can be ascribed to the C=O asymmetric stretch vibration of CO_2 and C-O antisymmetric stretching vibration of CO_3^{2-}, respectively[41]. Importantly, the absent signals of surface-adsorbed CO for the 2H/*fcc* $Au_{99}Cu_1$ (Fig. 4d), *i.e.*, the linear-bonded CO (CO_L) appeared between 2083 and 2079 cm^{-1} and the bridge-bonded CO (CO_B) located at 1831-1806 cm^{-1} (refs.[42]), have been detected on the surface of 2H/*fcc* $Au_{91}Cu_9$ (Fig. 4e). This observation indicates the weak adsorption/desorption interaction between the generated CO and the surface of 2H/*fcc* $Au_{99}Cu_1$, ensuring its high selectivity towards the CO production. In contrast, the adsorbed CO molecules on the 2H/*fcc* $Au_{91}Cu_9$ can be the key intermediate for the C-C coupling towards multi-carbon products, *e.g.*, C_2H_4, or hydrogenation towards CH_4 (ref.[43]). These results further confirm the distinct CO_2RR performance of the 2H/*fcc* $Au_{99}Cu_1$ and 2H/*fcc* $Au_{91}Cu_9$.

To reveal the intrinsic catalytic activities of the distinct catalysts, the electrochemically active surface area (ECSA) values of these catalysts were calculated to evaluate the number of their surface-active sites (Figs. S20 and S21)[44]. As shown in Fig. S21, compared to the 2H/*fcc* $Au_{91}Cu_9$ (135.7 cm^2) and *fcc* $Au_{99}Cu_1$ (85.7 cm^2), the 2H/*fcc* $Au_{99}Cu_1$ has the greatest ECSA value (150.0 cm^2), indicating the largest number of surface-active sites[44-46]. Subsequently, their intrinsic activities were evaluated by the comparison of their specific J_{CO}, which were obtained by normalizing their J_{CO} values to the corresponding ECSA values (Figs. S21 and S22). As shown in Fig. S22, in the applied potential window from -0.4 to -1.0 V (*vs.* RHE), the 2H/*fcc* $Au_{99}Cu_1$ exhibits

much higher specific activity compared to the 2H/*fcc* $Au_{91}Cu_9$ and *fcc* $Au_{99}Cu_1$. These results suggest that the superior performance of the 2H/*fcc* $Au_{99}Cu_1$ not only stems from the large number of surface-active sites but also arises from its high intrinsic activity.

The high intrinsic activity of 2H/*fcc* $Au_{99}Cu_1$ could be explained as follows. First, our previous reports have revealed that the *fcc*-2H-*fcc* Au nanorods with 2H phase and 2H/*fcc* phase boundaries could exhibit much higher selectivity and activity for electrochemical CO_2RR to CO compared with the *fcc* Au nanorods[25,26]. The excellent performance arises from the distinct atomic arrangement in the 2H phase and the unique 2H/*fcc* phase boundaries, which could endow the *fcc*-2H-*fcc* Au nanorods with energetically favorable adsorption of reaction intermediates[25]. Thus, our 2H/*fcc* $Au_{99}Cu_1$ with both 2H phase and 2H/*fcc* phase boundaries also contribute to the enhanced electrochemical performance for CO_2RR to CO. Second, the 2H/*fcc* $Au_{99}Cu_1$ possesses abundant high-index facets on the edges of both 2H and *fcc* domains. Previous studies have proven that the high-index facets of Au could exhibit abundant under-coordinated active sites, which are capable of improving the selectivity and activity of CO generation in CO_2RR[13]. Third, the planar defects, *e.g.*, stacking faults, twin boundaries, and grain boundaries, in 2H/*fcc* $Au_{99}Cu_1$ can also contribute to its superior intrinsic activity for CO_2RR to CO. In previous studies, the planar defects in Au nanomaterials could benefit the enhancement of their activity and selectivity for CO_2RR towards CO production[47-50]. Moreover, previous reports have proven that constructing AuCu bimetallic alloy with moderate content of oxophilic Cu could improve the interaction with the adsorbed COOH and thus facilitate the electrochemical

CO_2RR to CO compared to the pure Au nanostructures[6].

The long-term durability of the 2H/*fcc* $Au_{99}Cu_1$ in the H-type cell towards CO_2RR was evaluated by chronoamperometry. At a fixed current density of 6 mA cm^{-2}, the FE of CO of 2H/*fcc* $Au_{99}Cu_1$ still maintains as high as 91.4% and the potential shows negligible increase after 10 h testing (Fig. S23). Importantly, the hierarchical architecture, 2H/*fcc* heterophase, high-index facets, and planar defects of 2H/*fcc* $Au_{99}Cu_1$ have also been preserved after the stability testing (Fig. S24). The aforementioned results suggest that the 2H/*fcc* $Au_{99}Cu_1$ possesses excellent stability towards the electrochemical CO_2RR.

Due to the low solubility of CO_2 in conventional aqueous electrolytes, the mass transfer process in electrochemical CO_2RR is severely restricted, resulting in insufficient activity in the traditional H-type cell. In order to achieve the scaled-up production of CO at industrial current densities, a flow cell electrolyzer was utilized to conduct the electrochemical CO_2RR by using our 2H/*fcc* $Au_{99}Cu_1$ as cathodic catalyst (Fig. 5a). As shown in Fig. 5b, under a wide range of industry-relevant current densities, the 2H/*fcc* $Au_{99}Cu_1$ exhibits CO FEs of above 90%, indicating its tremendous potential for large-scale CO production. Impressively, at large current densities of 300 mA cm^{-2} and 500 mA cm^{-2}, the CO FEs of 2H/*fcc* $Au_{99}Cu_1$ are as high as 96.6% and 92.6%, respectively. The 2H/*fcc* $Au_{99}Cu_1$ with extraordinarily high FEs towards the CO production under industrial current densities places it among the best reported Au-based electrocatalysts for CO_2 reduction to produce CO in the flow cell (Table S2 and Fig. 5c) [32,51-59].

As another important indicator in CO_2RR, the long-term durability of the 2H/*fcc* $Au_{99}Cu_1$ was evaluated at an industrial current density of 300 mA cm^{-2} by using a membrane electrode assembly flow cell. As displayed in Fig. 5d, the cell voltage of 2H/*fcc* $Au_{99}Cu_1$ only shows negligible increase after the test for 17 h. More importantly, the selectivity of CO on the 2H/*fcc* $Au_{99}Cu_1$ catalyst can retain above 90% after testing for 17 h. These results reveal the good catalytic durability of the synthesized 2H/*fcc* $Au_{99}Cu_1$ during the electrochemical CO_2RR at large current density, showing its great potential in the future practical application.

Conclusion

In summary, we have successfully prepared novel AuCu nanostructures, *i.e.*, $Au_{99}Cu_1$ and $Au_{91}Cu_9$, possessing unconventional 2H/*fcc* heterophase, hierarchical architectures, high-index facets, and planar defects (*e.g.*, stacking faults, twin boundaries, and grain boundaries), *via* a facile one-pot wet-chemical method. Impressively, the 2H/*fcc* $Au_{99}Cu_1$ shows superior performance of CO_2RR towards the CO production, outperforming the 2H/*fcc* $Au_{91}Cu_9$, *fcc* $Au_{99}Cu_1$, and most reported Au-based electrocatalysts. *In situ* ATR-FTIR studies and other experimental results reveal that the unique structure features of 2H/*fcc* $Au_{99}Cu_1$, including the unconventional 2H/*fcc* heterophase, high-index facets, planar defects, and appropriate alloying of Cu, play essential roles in enhancing the CO_2RR performance. Furthermore, by using a flow cell electrolyzer, the 2H/*fcc* $Au_{99}Cu_1$ shows high CO FEs of over 90% at various industrial current densities up to 500 mA cm^{-2} as well as good durability, placing it among the best reported CO_2RR electrocatalysts for the CO production. Our delicately structural

modulation of nanomaterials based on the PEN strategy offers a promising way for the design and preparation of novel catalysts, especially with unconventional phase, to enhance their performances towards various sustainable catalytic reactions.

Notes

The authors declare no competing financial interest.

ACKNOWLEDGMENT

H.Z. thanks the support from the Research Grants Council of Hong Kong (TRS (T23-713/22-R)-Carbon Neutrality, AoE/P-701/20), ITC via the Hong Kong Branch of National Precious Metals Material Engineering Research Center (NPMM), and the Start-Up Grant (Project No. 9380100) and the grants (Project Nos. 7020054, 9678272 and 1886921) from the City University of Hong Kong.

References

(1) Shi, Y.; Lyu, Z.; Zhao, M.; Chen, R.; Nguyen, Q. N.; Xia, Y. Noble-metal nanocrystals with controlled shapes for catalytic and electrocatalytic applications. *Chem. Rev.* **2021**, *121*, 649-735.

(2) He, T.; Wang, W.; Shi, F.; Yang, X.; Li, X.; Wu, J.; Yin, Y.; Jin, M. Mastering the surface strain of platinum catalysts for efficient electrocatalysis. *Nature* **2021**, *598*, 76-81.

(3) Yang, C.-L.; Wang, L.-N.; Yin, P.; Liu, J.; Chen, M.-X.; Yan, Q.-Q.; Wang, Z.-S.; Xu, S.-L.; Chu, S.-Q.; Cui, C.; Ju, H.; Zhu, J.; Lin, Y.; Shui, J.; Liang, H.-W. Sulfur-anchoring synthesis of platinum intermetallic nanoparticle catalysts for fuel cells. *Science* **2021**, *374*, 459-464.

(4) Luo, M.; Zhao, Z.; Zhang, Y.; Sun, Y.; Xing, Y.; Lv, F.; Yang, Y.; Zhang, X.; Hwang, S.; Qin, Y.; Ma, J.-Y.; Lin, F.; Su, D.; Lu, G.; Guo, S. PdMo bimetallene for oxygen reduction catalysis. *Nature* **2019**, *574*, 81-85.

(5) Gilroy, K. D.; Ruditskiy, A.; Peng, H.-C.; Qin, D.; Xia, Y. Bimetallic nanocrystals: syntheses, properties, and applications. *Chem. Rev.* **2016**, *116*, 10414-10472.

(6) Kim, D.; Resasco, J.; Yu, Y.; Asiri, A. M.; Yang, P. Synergistic geometric and electronic effects for electrochemical reduction of carbon dioxide using gold–copper bimetallic nanoparticles. *Nat. Commun.* **2014**, *5*, 4948.

(7) Zhang, Z.; Liu, G.; Cui, X.; Gong, Y.; Yi, D.; Zhang, Q.; Zhu, C.; Saleem, F.; Chen, B.; Lai, Z.; Yun, Q.; Cheng, H.; Huang, Z.; Peng, Y.; Fan, Z.; Li, B.; Dai, W.; Chen, W.; Du, Y.; Ma, L.; Sun, C.-J.; Hwang, I.; Chen, S.; Song, L.; Ding, F.; Gu, L.; Zhu, Y.; Zhang, H. Evoking ordered vacancies in metallic nanostructures toward a vacated Barlow packing for high-performance hydrogen evolution. *Sci. Adv.* **2021**, *7*, eabd6647.

(8) Chen, Y.; Fan, Z.; Zhang, Z.; Niu, W.; Li, C.; Yang, N.; Chen, B.; Zhang, H. Two-dimensional metal nanomaterials: synthesis, properties, and applications. *Chem. Rev.* **2018**, *118*, 6409-6455.

(9) Wang, Y.; Wang, Z.; Dinh, C.-T.; Li, J.; Ozden, A.; Golam Kibria, M.; Seifitokaldani, A.; Tan, C.-S.; Gabardo, C. M.; Luo, M.; Zhou, H.; Li, F.; Lum, Y.; McCallum, C.; Xu, Y.; Liu, M.; Proppe, A.; Johnston, A.; Todorovic, P.; Zhuang, T.-T.; Sinton, D.; Kelley, S. O.; Sargent, E. H. Catalyst synthesis under CO_2

electroreduction favours faceting and promotes renewable fuels electrosynthesis. *Nat. Catal.* **2020**, *3*, 98-106.

(10) Yang, T.-H.; Ahn, J.; Shi, S.; Wang, P.; Gao, R.; Qin, D. Noble-metal nanoframes and their catalytic applications. *Chem. Rev.* **2021**, *121*, 796-833.

(11) Huang, L.; Liu, M.; Lin, H.; Xu, Y.; Wu, J.; Dravid Vinayak, P.; Wolverton, C.; Mirkin Chad, A. Shape regulation of high-index facet nanoparticles by dealloying. *Science* **2019**, *365*, 1159-1163.

(12) Choi, C.; Kwon, S.; Cheng, T.; Xu, M.; Tieu, P.; Lee, C.; Cai, J.; Lee, H. M.; Pan, X.; Duan, X.; Goddard, W. A.; Huang, Y. Highly active and stable stepped Cu surface for enhanced electrochemical CO_2 reduction to C_2H_4. *Nat. Catal.* **2020**, *3*, 804-812.

(13) Mezzavilla, S.; Horch, S.; Stephens, I. E. L.; Seger, B.; Chorkendorff, I. Structure sensitivity in the electrocatalytic reduction of CO_2 with gold catalysts. *Angew. Chem. Int. Ed.* **2019**, *58*, 3774-3778.

(14) Xie, C.; Niu, Z.; Kim, D.; Li, M.; Yang, P. Surface and interface control in nanoparticle catalysis. *Chem. Rev.* **2020**, *120*, 1184-1249.

(15) Wu, Z.; Wu, H.; Cai, W.; Wen, Z.; Jia, B.; Wang, L.; Jin, W.; Ma, T. Engineering bismuth–tin interface in bimetallic aerogel with a 3D porous structure for highly selective electrocatalytic CO_2 reduction to HCOOH. *Angew. Chem. Int. Ed.* **2021**, *60*, 12554-12559.

(16) Chen, Y.; Lai, Z.; Zhang, X.; Fan, Z.; He, Q.; Tan, C.; Zhang, H. Phase engineering of nanomaterials. *Nat. Rev. Chem.* **2020**, *4*, 243-256.

(17) Zhou, M.; Higaki, T.; Hu, G.; Sfeir, M. Y.; Chen, Y.; Jiang, D.-e.; Jin, R. Three-orders-of-magnitude variation of carrier lifetimes with crystal phase of gold nanoclusters. *Science* **2019**, *364*, 279-282.

(18) Zhao, M.; Xia, Y. Crystal-phase and surface-structure engineering of ruthenium nanocrystals. *Nat. Rev. Mater.* **2020**, *5*, 440-459.

(19) Huang, X.; Li, S.; Huang, Y.; Wu, S.; Zhou, X.; Li, S.; Gan, C. L.; Boey, F.; Mirkin, C. A.; Zhang, H. Synthesis of hexagonal close-packed gold nanostructures. *Nat. Commun.* **2011**, *2*, 292.

(20) Fan, Z.; Bosman, M.; Huang, X.; Huang, D.; Yu, Y.; Ong, K. P.; Akimov, Y. A.; Wu, L.; Li, B.; Wu, J.; Huang, Y.; Liu, Q.; Eng Png, C.; Lip Gan, C.; Yang, P.; Zhang, H. Stabilization of 4H hexagonal phase in gold nanoribbons. *Nat. Commun.* **2015**, *6*, 7684.

(21) Hong, J.; Bae, J.-H.; Jo, H.; Park, H.-Y.; Lee, S.; Hong, S. J.; Chun, H.; Cho, M. K.; Kim, J.; Kim, J.; Son, Y.; Jin, H.; Suh, J.-Y.; Kim, S.-C.; Roh, H.-K.; Lee, K. H.; Kim, H.-S.; Chung, K. Y.; Yoon, C. W.; Lee, K.; Kim, S. H.; Ahn, J.-P.; Baik, H.; Kim, G. H.; Han, B.; Jin, S.; Hyeon, T.; Park, J.; Son, C. Y.; Yang, Y.; Lee, Y.-S.; Yoo, S. J.; Chun, D. W. Metastable hexagonal close-packed palladium hydride in liquid cell TEM. *Nature* **2022**, *603*, 631-636.

(22) Zhang, X.; Luo, Z.; Yu, P.; Cai, Y.; Du, Y.; Wu, D.; Gao, S.; Tan, C.; Li, Z.; Ren, M.; Osipowicz, T.; Chen, S.; Jiang, Z.; Li, J.; Huang, Y.; Yang, J.; Chen, Y.; Ang, C. Y.; Zhao, Y.; Wang, P.; Song, L.; Wu, X.; Liu, Z.; Borgna, A.; Zhang, H. Lithiation-

induced amorphization of $Pd_3P_2S_8$ for highly efficient hydrogen evolution. *Nat. Catal.* **2018**, *1*, 460-468.

(23) Cheng, H.; Yang, N.; Liu, G.; Ge, Y.; Huang, J.; Yun, Q.; Du, Y.; Sun, C.-J.; Chen, B.; Liu, J.; Zhang, H. Ligand-exchange-induced amorphization of Pd nanomaterials for highly efficient electrocatalytic hydrogen evolution reaction. *Adv. Mater.* **2020**, *32*, 1902964.

(24) Zhou, X.; Ma, Y.; Ge, Y.; Zhu, S.; Cui, Y.; Chen, B.; Liao, L.; Yun, Q.; He, Z.; Long, H.; Li, L.; Huang, B.; Luo, Q.; Zhai, L.; Wang, X.; Bai, L.; Wang, G.; Guan, Z.; Chen, Y.; Lee, C.-S.; Wang, J.; Ling, C.; Shao, M.; Fan, Z.; Zhang, H. Preparation of Au@Pd core–shell nanorods with *fcc*-2H-*fcc* heterophase for highly efficient electrocatalytic alcohol oxidation. *J. Am. Chem. Soc.* **2022**, *144*, 547-555.

(25) Fan, Z.; Bosman, M.; Huang, Z.; Chen, Y.; Ling, C.; Wu, L.; Akimov, Y. A.; Laskowski, R.; Chen, B.; Ercius, P.; Zhang, J.; Qi, X.; Goh, M. H.; Ge, Y.; Zhang, Z.; Niu, W.; Wang, J.; Zheng, H.; Zhang, H. Heterophase *fcc*-2H-*fcc* gold nanorods. *Nat. Commun.* **2020**, *11*, 3293.

(26) Ge, Y.; Huang, Z.; Ling, C.; Chen, B.; Liu, G.; Zhou, M.; Liu, J.; Zhang, X.; Cheng, H.; Liu, G.; Du, Y.; Sun, C.-J.; Tan, C.; Huang, J.; Yin, P.; Fan, Z.; Chen, Y.; Yang, N.; Zhang, H. Phase-selective epitaxial growth of heterophase nanostructures on unconventional 2H-Pd nanoparticles. *J. Am. Chem. Soc.* **2020**, *142*, 18971-18980.

(27) Yang, N.; Cheng, H.; Liu, X.; Yun, Q.; Chen, Y.; Li, B.; Chen, B.; Zhang, Z.; Chen, X.; Lu, Q.; Huang, J.; Huang, Y.; Zong, Y.; Yang, Y.; Gu, L.; Zhang, H.

Amorphous/crystalline hetero-phase Pd nanosheets: one-pot synthesis and highly selective hydrogenation reaction. *Adv. Mater.* **2018**, *30*, 1803234.

(28) Lu, Q.; Wang, A.-L.; Gong, Y.; Hao, W.; Cheng, H.; Chen, J.; Li, B.; Yang, N.; Niu, W.; Wang, J.; Yu, Y.; Zhang, X.; Chen, Y.; Fan, Z.; Wu, X.-J.; Chen, J.; Luo, J.; Li, S.; Gu, L.; Zhang, H. Crystal phase-based epitaxial growth of hybrid noble metal nanostructures on 4H/*fcc* Au nanowires. *Nat. Chem.* **2018**, *10*, 456-461.

(29) Ge, Y.; Wang, X.; Chen, B.; Huang, Z.; Shi, Z.; Huang, B.; Liu, J.; Wang, G.; Chen, Y.; Li, L.; Lu, S.; Luo, Q.; Yun, Q.; Zhang, H. Preparation of *fcc*-2H-*fcc* heterophase Pd@Ir nanostructures for high-performance electrochemical hydrogen evolution. *Adv. Mater.* **2022**, *34*, 2107399.

(30) Gong, Z.; Liu, R.; Gong, H.; Ye, G.; Liu, J.; Dong, J.; Liao, J.; Yan, M.; Liu, J.; Huang, K.; Xing, L.; Liang, J.; He, Y.; Fei, H. Constructing a graphene-encapsulated amorphous/crystalline heterophase NiFe alloy by microwave thermal shock for boosting the oxygen evolution reaction. *ACS Catal.* **2021**, *11*, 12284-12292.

(31) Yin, P.-F.; Zhou, M.; Chen, J.; Tan, C.; Liu, G.; Ma, Q.; Yun, Q.; Zhang, X.; Cheng, H.; Lu, Q.; Chen, B.; Chen, Y.; Zhang, Z.; Huang, J.; Hu, D.; Wang, J.; Liu, Q.; Luo, Z.; Liu, Z.; Ge, Y.; Wu, X.-J.; Du, X.-W.; Zhang, H. Synthesis of palladium-based crystalline@amorphous core–shell nanoplates for highly efficient ethanol oxidation. *Adv. Mater.* **2020**, *32*, 2000482.

(32) Wang, J.; Yu, J.; Sun, M.; Liao, L.; Zhang, Q.; Zhai, L.; Zhou, X.; Li, L.; Wang, G.; Meng, F.; Shen, D.; Li, Z.; Bao, H.; Wang, Y.; Zhou, J.; Chen, Y.; Niu, W.; Huang, B.; Gu, L.; Lee, C.-S.; Fan, Z. Surface molecular functionalization of unusual phase

metal nanomaterials for highly efficient electrochemical carbon dioxide reduction under industry-relevant current density. *Small* **2022**, *18*, 2106766.

(33) Wang, X.; Ou, P.; Wicks, J.; Xie, Y.; Wang, Y.; Li, J.; Tam, J.; Ren, D.; Howe, J. Y.; Wang, Z.; Ozden, A.; Finfrock, Y. Z.; Xu, Y.; Li, Y.; Rasouli, A. S.; Bertens, K.; Ip, A. H.; Graetzel, M.; Sinton, D.; Sargent, E. H. Gold-in-copper at low *CO coverage enables efficient electromethanation of CO_2. *Nat. Commun.* **2021**, *12*, 3387.

(34) Kauffman, D. R.; Alfonso, D. R.; Tafen, D. N.; Wang, C.; Zhou, Y.; Yu, Y.; Lekse, J. W.; Deng, X.; Espinoza, V.; Trindell, J.; Ranasingha, O. K.; Roy, A.; Lee, J.-S.; Xin, H. L. Selective electrocatalytic reduction of CO_2 into CO at small, thiol-capped Au/Cu nanoparticles. *J. Phys. Chem. C* **2018**, *122*, 27991-28000.

(35) Wang, Y.; Zhou, W.; Jia, R.; Yu, Y.; Zhang, B. Unveiling the activity origin of a copper-based electrocatalyst for selective nitrate reduction to ammonia. *Angew. Chem. Int. Ed.* **2020**, *59*, 5350-5354.

(36) Dai, S.; Huang, T.-H.; Liu, W.-I.; Hsu, C.-W.; Lee, S.-W.; Chen, T.-Y.; Wang, Y.-C.; Wang, J.-H.; Wang, K.-W. Enhanced CO_2 electrochemical reduction performance over Cu@AuCu catalysts at high noble metal utilization efficiency. *Nano Lett.* **2021**, *21*, 9293-9300.

(37) Ma, X.; Shen, Y.; Yao, S.; Shu, M.; Si, R.; An, C. Self-supported nanoporous Au_3Cu electrode with enriched gold on surface for efficient electrochemical reduction of CO_2. *Chem. Eur. J.* **2020**, *26*, 4143-4149.

(38) Li, H.; Zeng, R.; Feng, X.; Wang, H.; Xu, W.; Lu, X.; Xie, Z.; Abruña, H. D. Oxidative stability matters: a case study of palladium hydride nanosheets for alkaline fuel cells. *J. Am. Chem. Soc.* **2022**, *144*, 8106-8114.

(39) Yuan, X.; Zhang, L.; Li, L.; Dong, H.; Chen, S.; Zhu, W.; Hu, C.; Deng, W.; Zhao, Z.-J.; Gong, J. Ultrathin Pd–Au shells with controllable alloying degree on Pd nanocubes toward carbon dioxide reduction. *J. Am. Chem. Soc.* **2019**, *141*, 4791-4794.

(40) Cao, Z.; Kim, D.; Hong, D.; Yu, Y.; Xu, J.; Lin, S.; Wen, X.; Nichols, E. M.; Jeong, K.; Reimer, J. A.; Yang, P.; Chang, C. J. A molecular surface functionalization approach to tuning nanoparticle electrocatalysts for carbon dioxide reduction. *J. Am. Chem. Soc.* **2016**, *138*, 8120-8125.

(41) Ross, S. D. Inorganic infrared and Raman spectra. *London: McGraw-Hill Book Company* **1972**, *140*.

(42) Zhang, G.; Zhao, Z.-J.; Cheng, D.; Li, H.; Yu, J.; Wang, Q.; Gao, H.; Guo, J.; Wang, H.; Ozin, G. A.; Wang, T.; Gong, J. Efficient CO_2 electroreduction on facet-selective copper films with high conversion rate. *Nat. Commun.* **2021**, *12*, 5745.

(43) Zheng, T.; Liu, C.; Guo, C.; Zhang, M.; Li, X.; Jiang, Q.; Xue, W.; Li, H.; Li, A.; Pao, C.-W.; Xiao, J.; Xia, C.; Zeng, J. Copper-catalysed exclusive CO_2 to pure formic acid conversion *via* single-atom alloying. *Nat. Nanotech.* **2021**, *16*, 1386-1393.

(44) Zhang, A.; He, R.; Li, H.; Chen, Y.; Kong, T.; Li, K.; Ju, H.; Zhu, J.; Zhu, W.; Zeng, J. Nickel doping in atomically thin tin disulfide nanosheets enables highly efficient CO_2 reduction. *Angew. Chem. Int. Ed.* **2018**, *57*, 10954-10958.

(45) Yang, F.; Elnabawy, A. O.; Schimmenti, R.; Song, P.; Wang, J.; Peng, Z.; Yao, S.; Deng, R.; Song, S.; Lin, Y.; Mavrikakis, M.; Xu, W. Bismuthene for highly efficient carbon dioxide electroreduction reaction. *Nat. Commun.* **2020**, *11*, 1088.

(46) Zhou, X.; Gao, H.; Wang, Y.; Liu, Z.; Lin, J.; Ding, Y. P vacancies-enriched 3D hierarchical reduced cobalt phosphide as a precursor template for defect engineering for efficient water oxidation. *J. Mater. Chem. A* **2018**, *6*, 14939-14948.

(47) Huang, H.; Zhao, J.; Weng, B.; Lai, F.; Zhang, M.; Hofkens, J.; Roeffaers, M. B. J.; Steele, J. A.; Long, J. Site-sensitive selective CO_2 photoreduction to CO over gold nanoparticles. *Angew. Chem. Int. Ed.* **2022**, *61*, e202204563.

(48) Mariano, R. G.; McKelvey, K.; White, H. S.; Kanan, M. W. Selective increase in CO_2 electroreduction activity at grain-boundary surface terminations. *Science* **2017**, *358*, 1187-1192.

(49) Feng, X.; Jiang, K.; Fan, S.; Kanan, M. W. Grain-boundary-dependent CO_2 electroreduction activity. *J. Am. Chem. Soc.* **2015**, *137*, 4606-4609.

(50) Kim, K.-S.; Kim, W. J.; Lim, H.-K.; Lee, E. K.; Kim, H. Tuned chemical bonding ability of Au at grain boundaries for enhanced electrochemical CO_2 reduction. *ACS Catal.* **2016**, *6*, 4443-4448.

(51) Verma, S.; Hamasaki, Y.; Kim, C.; Huang, W.; Lu, S.; Jhong, H.-R. M.; Gewirth, A. A.; Fujigaya, T.; Nakashima, N.; Kenis, P. J. A. Insights into the low overpotential electroreduction of CO_2 to CO on a supported gold catalyst in an alkaline flow electrolyzer. *ACS Energy Lett.* **2018**, *3*, 193-198.

(52) Monteiro, M. C. O.; Philips, M. F.; Schouten, K. J. P.; Koper, M. T. M. Efficiency and selectivity of CO_2 reduction to CO on gold gas diffusion electrodes in acidic media. *Nat. Commun.* **2021**, *12*, 4943.

(53) Jhong, H.-R. M.; Tornow, C. E.; Kim, C.; Verma, S.; Oberst, J. L.; Anderson, P. S.; Gewirth, A. A.; Fujigaya, T.; Nakashima, N.; Kenis, P. J. A. Gold nanoparticles on polymer-wrapped carbon nanotubes: an efficient and selective catalyst for the electroreduction of CO_2. *ChemPhysChem* **2017**, *18*, 3274-3279.

(54) Qi, Z.; Biener, M. M.; Kashi, A. R.; Hunegnaw, S.; Leung, A.; Ma, S.; Huo, Z.; Kuhl, K. P.; Biener, J. Electrochemical CO_2 to CO reduction at high current densities using a nanoporous gold catalyst. *Mater. Res. Lett.* **2021**, *9*, 99-104.

(55) Sun, K.; Shi, Y.; Li, H.; Shan, J.; Sun, C.; Wu, Z.-y.; Ji, Y.; Wang, Z. Efficient CO_2 electroreduction *via* Au-complex derived carbon nanotube supported Au nanoclusters. *ChemSusChem* **2021**, *14*, 4929-4935.

(56) Seong, H.; Efremov, V.; Park, G.; Kim, H.; Yoo, J. S.; Lee, D. Atomically precise gold nanoclusters as model catalysts for identifying active sites for electroreduction of CO_2. *Angew. Chem. Int. Ed.* **2021**, *60*, 14563-14570.

(57) Yin, Z.; Peng, H.; Wei, X.; Zhou, H.; Gong, J.; Huai, M.; Xiao, L.; Wang, G.; Lu, J.; Zhuang, L. An alkaline polymer electrolyte CO_2 electrolyzer operated with pure water. *Energy Environ. Sci.* **2019**, *12*, 2455-2462.

(58) Ozden, A.; Liu, Y.; Dinh, C.-T.; Li, J.; Ou, P.; García de Arquer, F. P.; Sargent, E. H.; Sinton, D. Gold adparticles on silver combine low overpotential and high

selectivity in electrochemical CO_2 conversion. *ACS Appl. Energy Mater.* **2021**, *4*, 7504-7512.

(59) Fenwick, A. Q.; Welch, A. J.; Li, X.; Sullivan, I.; DuChene, J. S.; Xiang, C.; Atwater, H. A. Probing the catalytically active region in a nanoporous gold gas diffusion electrode for highly selective carbon dioxide reduction. *ACS Energy Lett.* **2022**, *7*, 871-879.

Figs.

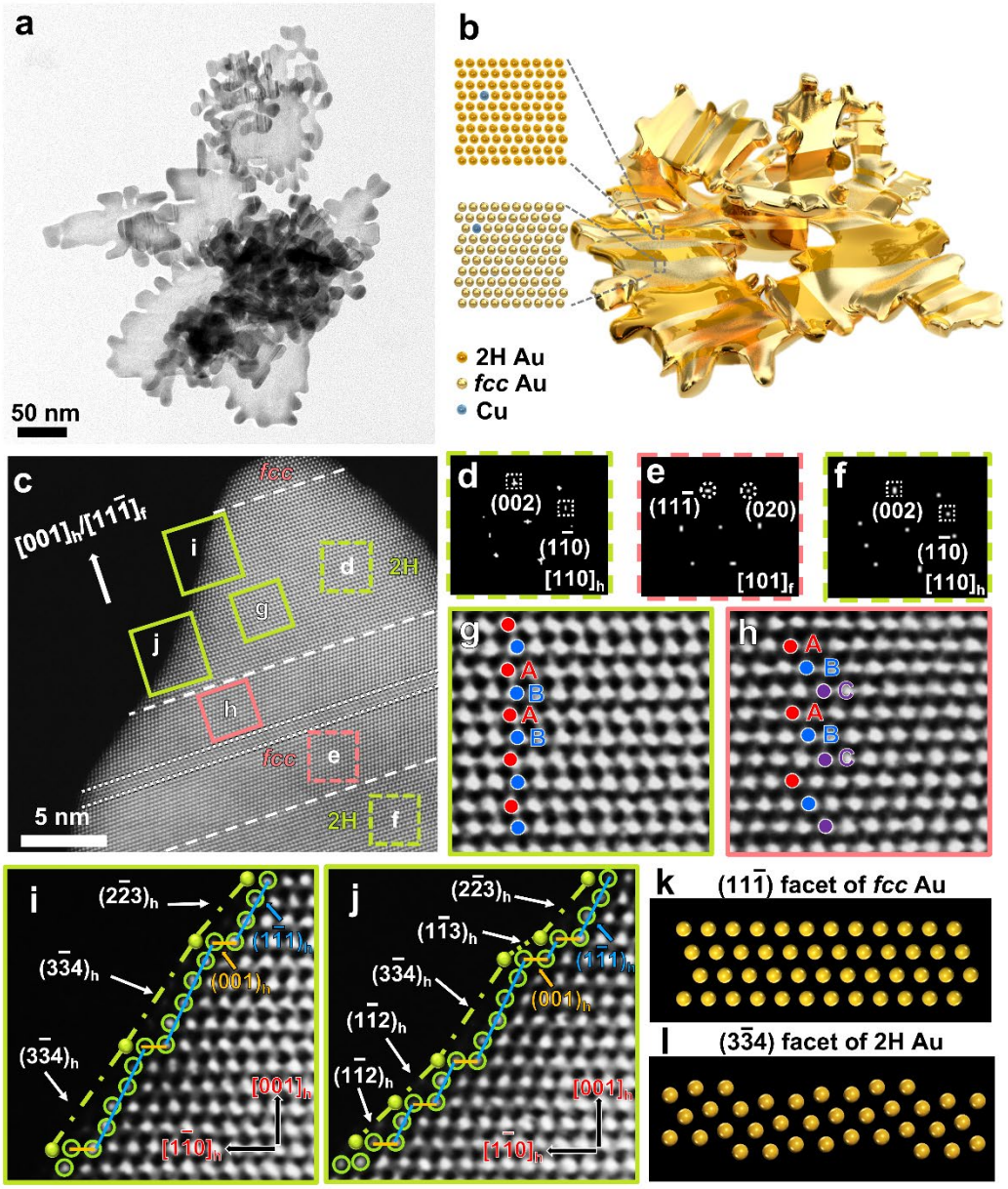

Fig. 1 Structural analysis of 2H/*fcc*-heterophase $Au_{99}Cu_1$. a, TEM image of a representative 2H/*fcc* $Au_{99}Cu_1$. **b**, Schematic illustration of a 2H/*fcc* $Au_{99}Cu_1$. **c**, A representative aberration-corrected high-resolution HAADF-STEM image of a protrusion at edge of 2H/*fcc* $Au_{99}Cu_1$. The 2H/*fcc* phase boundaries are marked with white dash lines. The twin boundaries are marked with white dotted lines. **d-f**, FFT patterns of the corresponding 2H (d,f) and *fcc* (e) areas of the 2H/*fcc* $Au_{99}Cu_1$ in c. **g**,**h**, The high-magnification HAADF-STEM image taken from the corresponding areas in c. **i**,**j**, The high-magnification HAADF-STEM image taken from the corresponding edge areas in c. The high index facets in the 2H domain are marked with green dashed-dotted lines. **k**,**l**, The side-view models of the (11$\bar{1}$) facet of *fcc* Au (k) and (3$\bar{3}$4) facet of 2H Au (l).

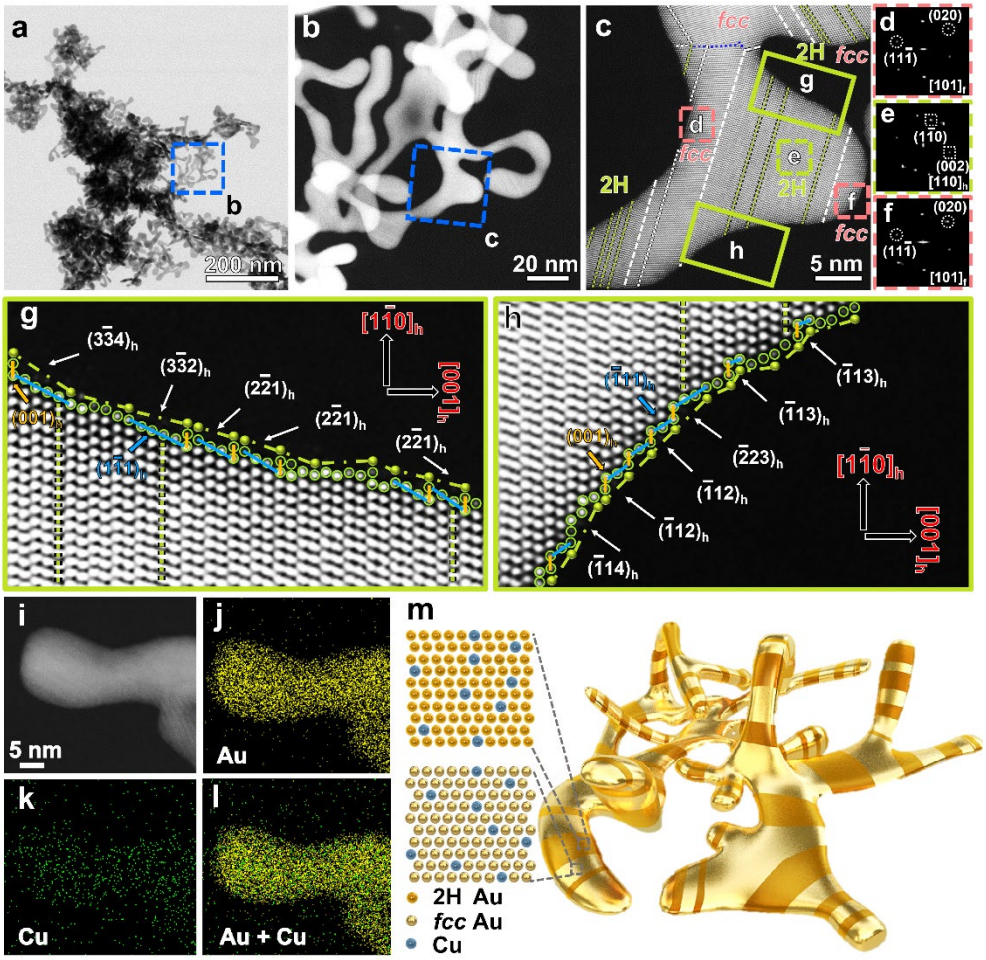

Fig. 2. Structural analysis of 2H/*fcc*-heterophase $Au_{91}Cu_9$. a, TEM image of synthesized 2H/*fcc* $Au_{91}Cu_9$. **b,** High-magnification dark-field STEM image of the 2H/*fcc* $Au_{99}Cu_1$ taken from selected area in (a). **c,** A representative aberration-corrected high-resolution HAADF-STEM image of the 2H/*fcc* $Au_{91}Cu_9$ taken from selected area in (b). The 2H/*fcc* phase boundaries are marked with white dash lines. The stacking faults, twin boundaries, and grain boundaries in the 2H/*fcc* $Au_{91}Cu_9$ are marked with green, white, and blue dotted lines, respectively. **d-f**, FFT patterns of the corresponding *fcc* (d,f) and 2H (e) areas of the 2H/*fcc* $Au_{91}Cu_9$ in (c). **g**,**h**, The high-magnification HAADF-STEM images taken from the edge areas in c. The stacking faults in the 2H domain are marked with green dotted lines. The high index facets in the 2H domain are marked with green dashed-dotted lines. **i-l**, HAADF-STEM image (i) and the corresponding EDS elemental mappings (j-l) of the 2H/*fcc* $Au_{91}Cu_9$. **m**, Schematic illustration of the 2H/*fcc* $Au_{91}Cu_9$.

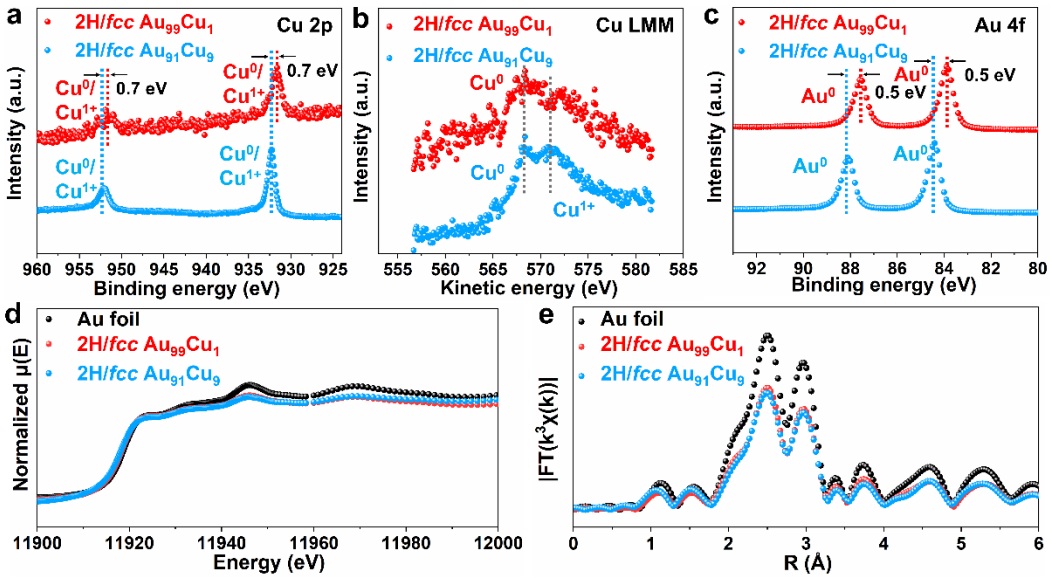

Fig. 3 X-ray spectral analyses of 2H/*fcc*-heterophase AuCu nanostructures. a, Cu 2p XPS spectra, **b**, Cu LMM AES spectra, and **c**, Au 4f XPS spectra of the 2H/*fcc* $Au_{99}Cu_1$ and 2H/*fcc* $Au_{91}Cu_9$. **d**, XANES and **e**, FT-EXAFS spectra of the 2H/*fcc* $Au_{99}Cu_1$, 2H/*fcc* $Au_{91}Cu_9$, and Au foil.

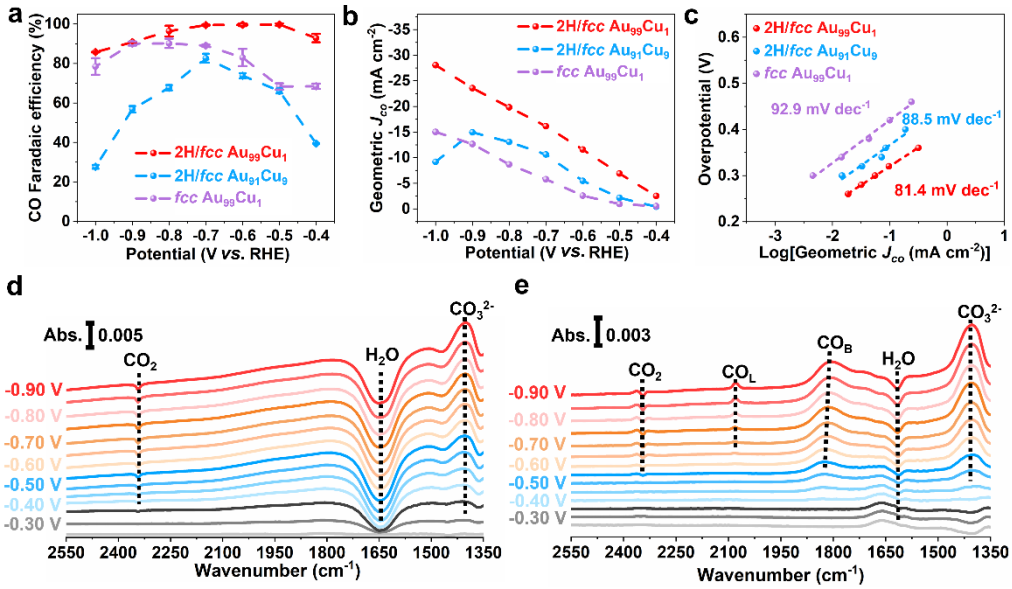

Fig. 4 Performance and mechanism studies of Au-based catalysts for the electrochemical CO_2RR. a, CO FEs of 2H/*fcc* $Au_{99}Cu_1$, 2H/*fcc* $Au_{91}Cu_9$ and *fcc* $Au_{99}Cu_1$ at different applied potentials. **b**, Partial CO current densities normalized to the geometric surface area of carbon-paper electrodes for different catalysts. **c**, Tafel plots of different catalysts. **d**,**e**, *In situ* ATR-FTIR results recorded during electrochemical CO_2RR on the 2H/*fcc* $Au_{99}Cu_1$ (d) and 2H/*fcc* $Au_{91}Cu_9$ (e) in CO_2-saturated 0.5 M $KHCO_3$ aqueous solution.

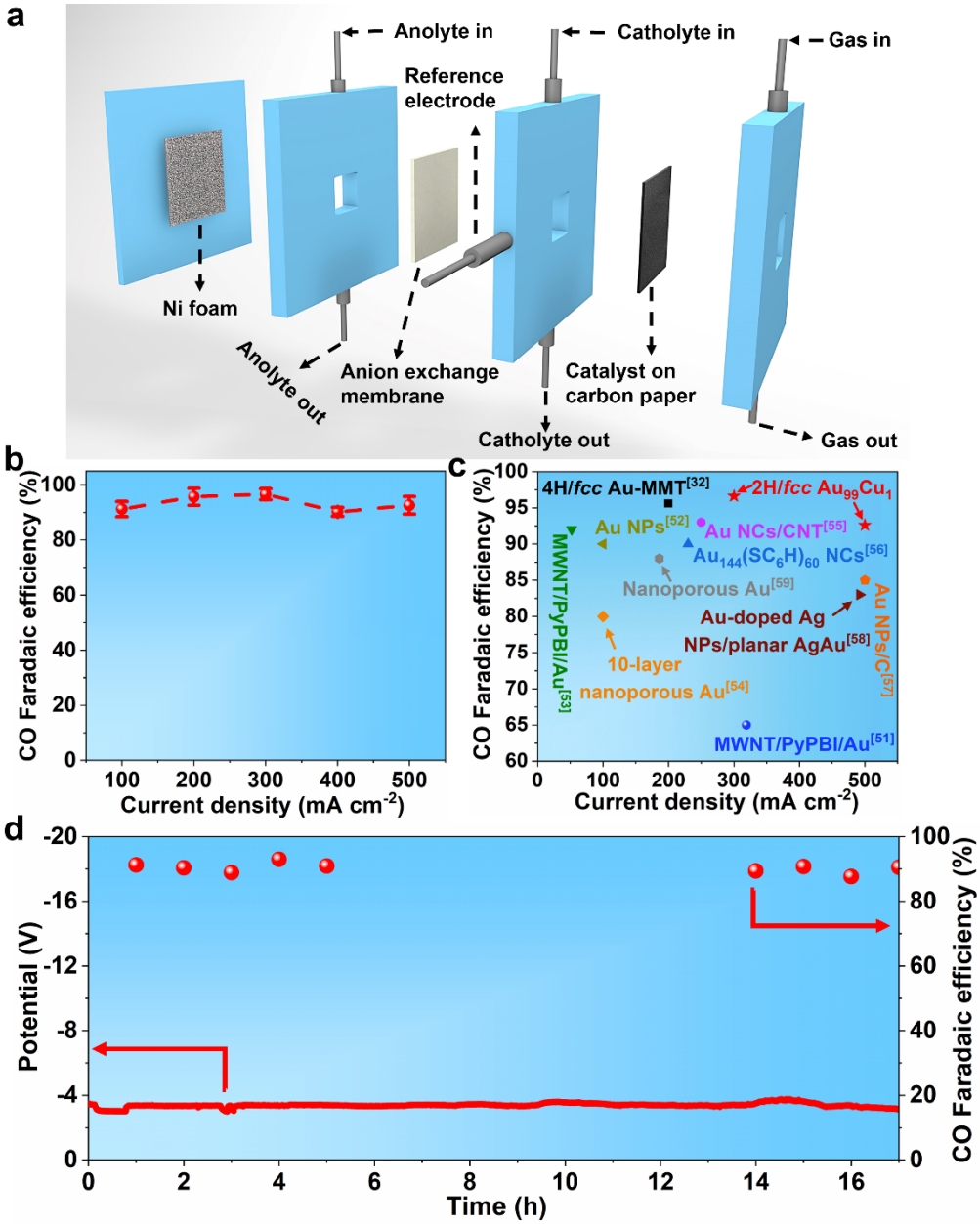

Fig. 5 Electrocatalytic CO_2RR using 2H/*fcc* $Au_{99}Cu_1$ in flow cell at industrial current densities. a, Schematic illustration of the flow cell electrolyzer. **b**, CO FEs of 2H/*fcc* $Au_{99}Cu_1$ in 1.0 M KOH aqueous solution at different current densities. **c**, Comparison of the CO_2RR performance of the 2H/*fcc* $Au_{99}Cu_1$ with some previously reported representative Au-based electrocatalysts. **d**, Long-term durability test of the 2H/*fcc* $Au_{99}Cu_1$ at an industrial current density of 300 mA cm^{-2}.

TOC

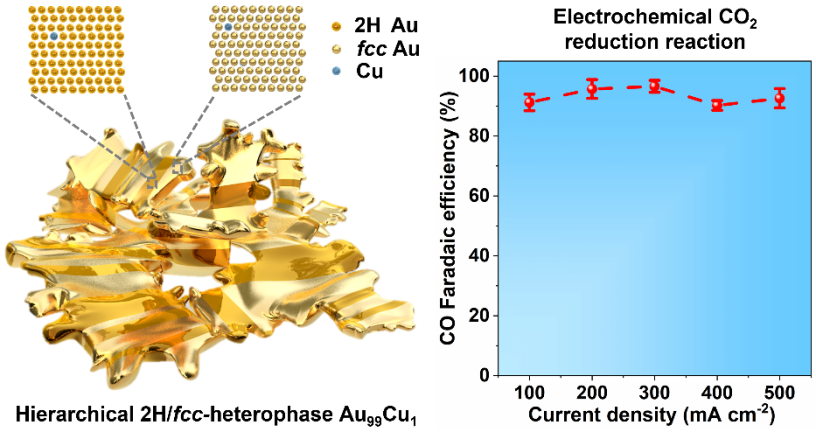
2H Au
fcc Au
Cu
Hierarchical 2H/fcc-heterophase Au99Cu1
Electrochemical CO2 reduction reaction
CO Faradaic efficiency (%)
0
20
40
60
80
100
100
200
300
400
500
Current density (mA cm-2)